Journal of Virology

A Ribosome-Binding, 3′ Translational Enhancer Has a T-Shaped Structure and Engages in a Long-Distance RNA-RNA Interaction

Feng Gao, Wojciech Kasprzak, Vera A. Stupina, Bruce A. Shapiro and Anne E. Simon

J. Virol. **2012, 86(18):9828. DOI: 10.1128/JVI.00677-12.**
Published Ahead of Print 3 July 2012.

JVI Journals.ASM.org

A Ribosome-Binding, 3′ Translational Enhancer Has a T-Shaped Structure and Engages in a Long-Distance RNA-RNA Interaction

Feng Gao,[a] Wojciech Kasprzak,[b] Vera A. Stupina,[a] Bruce A. Shapiro,[c] and Anne E. Simon[a]

Department of Cell Biology and Molecular Genetics, University of Maryland—College Park, College Park, Maryland, USA[a]; Basic Science Program, SAIC—Frederick, Inc., Center for Cancer Research Nanobiology Program, Frederick National Laboratory for Cancer Research, Frederick, Maryland, USA[b]; and Center for Cancer Research Nanobiology Program, National Cancer Institute, Frederick National Laboratory for Cancer Research, Frederick, Maryland, USA[c]

Many plant RNA viruses contain elements in their 3′ untranslated regions (3′ UTRs) that enhance translation. The PTE (*Panicum mosaic virus*-like translational enhancer) of *Pea enation mosaic virus* (PEMV) binds to eukaryotic initiation factor 4E (eIF4E), but how this affects translation from the 5′ end is unknown. We have discovered a three-way branched element just upstream of the PEMV PTE that engages in a long-distance kissing-loop interaction with a coding sequence hairpin that is critical for the translation of a reporter construct and the accumulation of the viral genome *in vivo*. Loss of the long-distance interaction was more detrimental than elimination of the adjacent PTE, indicating that the RNA-RNA interaction supports additional translation functions besides relocating the PTE to the 5′ end. The branched element is predicted by molecular modeling and molecular dynamics to form a T-shaped structure (TSS) similar to the ribosome-binding TSS of *Turnip crinkle virus* (TCV). The PEMV element binds to plant 80S ribosomes with a K_d (dissociation constant) of 0.52 μM and to 60S subunits with a K_d of 0.30 μM. Unlike the TCV TSS, the PEMV element also binds 40S subunits (K_d, 0.36 μM). Mutations in the element that suppressed translation reduced either ribosome binding or the RNA-RNA interaction, suggesting that ribosome binding is important for function. This novel, multifunctional element is designated a kl-TSS (kissing-loop T-shaped structure) to distinguish it from the TCV TSS. The kl-TSS has sequence and structural features conserved with the upper portion of most PTE-type elements, which, with the exception of the PEMV PTE, can engage in similar long-distance RNA-RNA interactions.

In eukaryotic cells, virtually all nuclearly transcribed mRNAs possess a 5′ m7GpppN cap and a 3′ poly(A) tail for recruiting translation initiation factors and ribosomal subunits, leading to initiation of translation, the rate-limiting step in protein biosynthesis (15, 39). The 5′ cap is bound by initiation factor 4E (eIF4E), which, along with scaffold protein eIF4G and helicase/ATPase eIF4A, is a subunit of eIF4F. eIF4G recruits the 43S preinitiation complex through binding to associated factor eIF3 and also contributes to circularizing the mRNA by interacting with 3′ poly(A)-bound PABP (33, 38, 50). Following recruitment to the template, the 43S complex transits along the mRNA in the 5′-to-3′ direction until it encounters an initiation codon in a favorable context where initiation factors dissociate, 60S subunits join to assemble the 80S ribosome, and translation initiation commences.

Posttranscriptional control of gene expression is estimated to contribute as much as two-thirds to the steady-state level of cellular proteins (1, 45, 46). Translational control elements in the 5′ untranslated region (5′ UTR) that impede cap-dependent ribosome access to the initiation codon are widespread and can include highly stable RNA secondary structures, short coding regions, and *cis*-acting protein-binding elements (15, 39, 44). The 3′ UTR, which is generally substantially longer than the 5′ UTR, is also a repository for a variety of *cis* elements that influence translation. While some 3′ UTR elements affect translation by specifying the subcellular localization and stability of the mRNA, others suppress translation by being target sites for repression by small RNAs (22) or by interfering with 5′-3′ circularization through interactions between specific motifs and RNA binding proteins (7, 19). More rare are 3′ elements [other than the poly(A) tail] that enhance translation using mechanisms that are poorly understood (28, 30).

Many RNA viruses have evolved to dispense with 5′ caps and/or 3′ poly(A) tails so as to differentially compete with host mRNAs or permit viral translation when producing proteins that inhibit cap-dependent translation by inactivating initiation factors. Most animal positive-strand RNA viruses lacking 5′ caps contain large (~200- to 450-nucleotide [nt]), highly structured internal ribosome entry sites (IRESs) in or near their 5′ UTRs that bind to the 40S subunit with a reduced need for translation initiation factors (8, 11, 25). The compact size of most plant virus 5′ UTRs limits the inclusion of large animal virus-type IRESs, and elements that bind translation initiation factors and significantly enhance translation are localized mainly to the 3′ UTR and nearby coding regions (9, 18, 29, 30). Although the sequence and structure of plant virus 3′ cap-independent translation enhancers (3′ CITEs) differ significantly, most contain a hairpin with an apical loop that is known or predicted to engage in a long-distance RNA-RNA kissing-loop interaction with 5′ hairpins, which is thought to relocalize bound initiation factors to the 5′ end to support 40S recruitment (5, 29, 31).

A unique 3′ CITE was recently discovered in the 3′ UTR of the carmovirus *Turnip crinkle virus* (TCV). The TCV 3′ CITE folds into a T-shaped structure (TSS) that binds to the P-site of 80S ribosomes and 60S subunits (26, 41, 57). Ribosome binding is required for CITE activity, as are upstream sequences and struc-

Received 16 March 2012 Accepted 25 June 2012
Published ahead of print 3 July 2012
Address correspondence to Bruce A. Shapiro, shapirbr@mail.nih.gov, and Anne E. Simon, simona@umd.edu.

doi:10.1128/JVI.00677-12

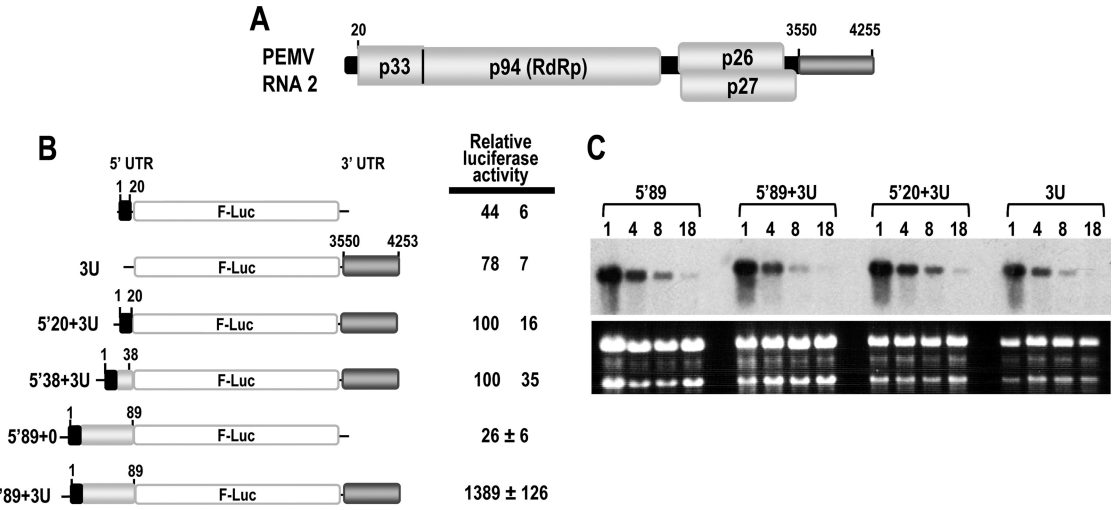

FIG 1 The 5′89 fragment of PEMV contributes to translational enhancement mediated by the 3′ UTR. (A) Genome organization of PEMV RNA-2. (B) Regions involved in PEMV translation. gRNA constructs contained either the gRNA 5′ UTR (positions 1 to 20) or extended 5′ sequences (positions 1 to 38 or 1 to 89) at the 5′ end and the exact 3′ UTR at the 3′ end. Filled rectangles represent the 5′ UTR sequence, and light shaded rectangles represent coding sequence. The medium shaded rectangle represents the full-length 3′ UTR. Transcripts were inoculated into *A. thaliana* protoplasts along with transcripts from a control R-Luc construct, and luciferase levels were assayed 18 h later. The standard deviation for three replicate experiments is shown. (C) Stability of selected reporter transcripts. Transcripts were transfected into protoplasts, and levels remaining at 4, 8, and 18 hpi were determined by Northern blot analysis. rRNA levels are shown below the autoradiogram.

tures (41, 52–54). No RNA-RNA interactions link the TCV 5′ and 3′ UTRs, implying that an alternative mechanism exists to circularize the genome and transfer the bound ribosome or ribosomal subunits to the 5′ end. A recent report suggests that the ribosome itself may contribute to circularizing the genome through the simultaneous binding of the 40S subunit to a pyrimidine-rich sequence in the 5′ UTR and the 60S subunit to the 3′ UTR TSS (42).

The existence of a ribosome binding element in the 3′ UTR of TCV prompted a search for similar elements in other viral genomes. *Pea enation mosaic virus* (PEMV) is composed of two taxonomically distinct single-stranded plus-strand RNAs that were once independent viruses (37). PEMV RNA-2 (4,052 nt), which belongs to the genus *Umbravirus*, has no 5′ cap or 3′ poly(A) tail, can independently infect single cells, and relies on RNA-1 for coat protein synthesis, encapsidation, and transmission (35). PEMV RNA-2 (referred to below as PEMV) contains four open reading frames (ORFs) (Fig. 1), one of which encodes a carmovirus-like RNA-dependent RNA polymerase (RdRp) (94 kDa) (6). The PEMV 3′ UTR contains a branched 3′ CITE (PTE [*Panicum mosaic virus*-like translational enhancer]) (48, 49) similar to structures found in the panicovirus *Panicum mosaic virus* (PMV) (2) and seven carmoviruses, including *Saguaro cactus virus* (SCV) (5). The PEMV PTE binds to eIF4E, but in contrast to other PTEs (5), no associated RNA-RNA interactions were identified that could position the eIF4E-bound PTE near the 5′ end of the viral templates. We now report that PEMV contains a second 3′ CITE just upstream of the PTE that engages in a long-distance kissing-loop interaction with a coding region hairpin and binds to 80S ribosomes and both large and small ribosomal subunits. This element thus represents a novel translational enhancer that combines the ribosome-binding activity of the TCV TSS with the long-distance RNA-RNA interaction activity of PTE and other plant RNA virus 3′ CITEs.

MATERIALS AND METHODS

Construction of PEMV mutants and synthesis of RNA transcripts. Oligonucleotide-mediated site-directed mutagenesis was used along with PCR to generate 3′ UTR mutants in pUC19-PEMV, which contains the full-length wild-type (wt) PEMV RNA-2 sequence downstream from a T7 RNA polymerase promoter. PCR fragments were designed for digestion with EcoRI and SmaI and were used to replace the wt fragments in the constructs. Mutations in fragments 5′89 and F6 were generated from the corresponding pUC19-PEMV mutant constructs using PCR with a 5′ primer that contained a T7 RNA polymerase promoter. *In vitro* transcription was carried out as described previously (52).

EMSA. RNA-RNA electrophoretic mobility gel shift assays (EMSAs) were performed essentially as described previously (31). 5′-end-labeled [γ-^{32}P]ATP RNA and unlabeled RNA were heated separately to 75°C and were slowly cooled to room temperature. End-labeled RNA (2 pmol) was incubated for 30 min at 25°C with 20 pmol of unlabeled RNA in RNA binding buffer (5 mM HEPES [pH 7.6], 100 mM KCl, 10 mM $MgCl_2$, 0.1 mM EDTA, 3.8% glycerol). For competition assays, the competing RNA was also heated and slow-cooled and was then added in a molar ratio ranging from 1- to 10-fold. Reaction products were then snap-cooled on ice and were subjected to electrophoresis through a 10% native polyacrylamide gel at 4°C for 4 to 5 h in 1× THEM buffer (34 mM Tris, 66 mM HEPES [pH 7.5], 10 mM $MgCl_2$, 0.1 mM EDTA). For the ribosome-binding EMSAs, 5′-end-labeled [γ-^{32}P]ATP RNA (3 pmol) was incubated together with competing RNA and 80S ribosomes (12 pmol) at 25°C for 30 min in ribosome binding buffer [80 mM Tris-HCl (pH 7.4), 160 mM NH_4Cl, 11 mM $Mg(CH_3COO)_2$, 6 mM β-mercaptoethanol, 0.4 mM GTP, 2 mM spermidine, 0.4 μg/ml poly(U)]. Reaction products were then resolved by native composite gels (0.5% agarose and 3% acrylamide) at 4°C in 1× TBM buffer [89 mM Tris, 89 mM boric acid, 10 mM $Mg(CH_3COO)_2$]. After electrophoresis, gels were dried and exposed to X-ray film.

In-line structure probing. In-line probing was performed as described previously (26, 53). Transcripts synthesized using T7 RNA polymerase were 5′ end labeled with [γ-^{32}P]ATP and were then purified by electrophoresis through 5% denaturing polyacrylamide gels. RNA cleav-

age ladders were generated by incubating end-labeled RNA in a reaction mixture containing 1.5 μg yeast tRNA, 50 mM $NaHCO_3$–Na_2CO_3 (pH 9.2), and 1 mM EDTA for 5 min at 95°C. RNase T1 digestions were carried out by incubating 5 pmol of denatured, radiolabeled RNA with 2 μg of yeast tRNA, 20 mM sodium citrate (pH 5.0), 1 mM EDTA, 7 M urea, and 1 U RNase T1 for 5 min at 25°C. For in-line probing, a typical reaction mixture containing 5 pmol of end-labeled RNA in 50 mM Tris-HCl (pH 8.5) and 20 mM $MgCl_2$ was allowed to self-cleave at 25°C for 14 h. Unlabeled RNA fragments were added in a 10-fold molar excess. At least three independent in-line probing assays were performed, and only reproducible differences are described.

Accumulation of PEMV in protoplasts. Protoplasts were prepared from callus cultures of *Arabidopsis thaliana* (ecotype Col-0) as described previously (55). Protoplasts (5×10^6) were inoculated with 20 μg of PEMV genomic RNA (gRNA) transcripts, and total RNA was extracted at 24 h postinoculation (hpi). RNA (2 μg) was subjected to reverse transcription in a 20-μl reaction volume using Moloney murine leukemia virus (MMLV) reverse transcriptase (Invitrogen). The resulting cDNA was then subjected to TaqMan real-time PCR assays using a LightCycler 480 real-time PCR system (Roche Applied Science). 6-Carboxyfluorescein (FAM)-labeled probes for target genes (probe 024, catalogue no. 04686985001) and internal control genes (*Arabidopsis* ACT2) (probe 120; catalogue no. 04693540001) were designed in the Roche Applied Science Universal Probe Library Assay Design Center. The reaction mixture contained 0.5 μM gene-specific primers, 0.1 μM TaqMan gene-specific probe, and 1× LightCycler 480 Probe Master (Roche Applied Science). Thermal cycling conditions included a denaturation step for 5 min at 95°C followed by 45 cycles consisting of 2 steps: 95°C for 5 s and 60°C for 30 s for annealing and extension. The raw data were analyzed using LightCycler 480 real-time PCR system software. Each sample was assayed in triplicate, and at least three independent experiments were performed.

***In vivo* translation assays.** Uncapped wt and mutant transcripts (30 μg) were inoculated into *A. thaliana* protoplasts using 50% polyethylene glycol (PEG) along with 10 μg of a control, uncapped *Renilla* luciferase (R-Luc) transcripts, and luciferase levels were assayed 18 h later using a Modulus microplate multimode reader (Turner BioSystems), as described previously (42).

Molecular modeling. Three-dimensional (3-D) structure modeling was performed with the RNA2D3D and MCSym programs (24, 32).

Molecular dynamic simulations. Molecular dynamic (MD) simulations were performed with Amber 10, employing the Cornell force field for RNA, and the particle-mesh Ewald summation method to calculate the electrostatic interactions (4, 12, 47). A cutoff of 9 Å was used for the nonbonded interactions. Prior to solvation, the RNAs were subjected to energy minimization runs, and the minimized molecules were then solvated as described below. Structures consisting of one 71-nt chain used 70 Na^+ neutralizing ions. Neutralized RNA molecules were placed in solvent boxes, with explicit TIP3P water molecules and additional Na^+-Cl^- ion pairs added to solvate the system to a relative salt concentration of 0.1 mol/liter. The equilibration protocol consisted of multiple stages in which constraints were initially imposed on the RNA while the solvent was being equilibrated and were then slowly released to equilibrate the entire system at 300K; this temperature was maintained throughout all MD production runs using the Berendsen thermostat (3). The last phase of the equilibration without any restraints on the RNA lasted 80 ps. The SHAKE algorithm was applied to all hydrogen bonds in the system. Pressure was maintained at 1.0 Pa using the Berendsen algorithm (3), and a periodic boundary condition was imposed. Following equilibration, production simulation was performed with 2-fs time steps for a total of 50 to 63 ns, depending on the total system size. Because of the different shapes of the "T" and "Y" initial F6 element models (the Y's being more compact than the T's), the total sizes of the systems subjected to MD ranged from 42,000 to 57,000 atoms. For all systems, the solvent boxes were devised with a clearance distance of 10 Å (the minimum distance between the solute and the solvent box wall, also referred to as "buffer" in Amber nomenclature). Analyses of the MD results were performed using the ptraj module of Amber, with the equilibration stage results excluded.

Isolation of 80S ribosomes and 40S and 60S ribosomal subunits from *Arabidopsis thaliana* protoplasts and binding assays. A new procedure (unpublished data) was developed to isolate plant ribosomes with high yields and quality. *Arabidopsis thaliana* protoplasts, prepared from callus cultures as described above, were used as the plant source for the preparation of ribosomes. Protoplasts were passively lysed by gentle rocking of the lysate for 5 min. Cellular debris was pelleted by centrifugation at 10,000 × *g*, and ribosomes were sedimented by centrifugation of the supernatant through a 25% glycerol cushion at 4°C for 3 h at 50,000 rpm using an MSL-50 rotor (Beckman). Ribosomal pellets were washed and resuspended at concentrations of 2 to 10 pmol/μl in storage buffer [50 mM HEPES-KOH (pH 7.6), 5 mM $Mg(CH_3COO)_2$, 50 mM NH_4Cl, 25% glycerol, 1 mM dithiothreitol (DTT)]. Ribosomes were salt-washed using a procedure for the preparation of salt-washed yeast ribosomes, as described previously (26). To isolate plant 40S and 60S ribosomal subunits, purified plant 80S ribosomes were subjected to sucrose gradient centrifugation as described previously for the isolation of yeast ribosomal subunits (42). Fractions containing plant 40S and 60S ribosomal subunits were collected into two pools, and each pool was applied to an Amicon Ultra (100k) column (Millipore) for buffer exchange and sample concentration against 50 mM HEPES-KOH (pH 7.6), 5 mM $Mg(CH_3COO)_2$, 50 mM NH_4Cl, 10% glycerol, and 1 mM DTT. Following the addition of glycerol to a final concentration of 25%, ribosomes and ribosomal subunits were stored at −80°C. Filter binding assays were performed as described previously (41).

RESULTS

A long-distance RNA-RNA interaction occurs between an element located upstream of the PTE and a 5′ coding region hairpin. A previous report found no evidence for any RNA-RNA interactions between the 5′ UTR (20 nt) and the 3′ UTR (702 nt) of PEMV (49), provoking the question of how the eIF4E-binding, 3′-proximal PTE participates in translation initiating from the 5′ end. To investigate if the PEMV PTE or another 3′ UTR element is capable of engaging in a long-distance RNA-RNA interaction with coding sequences proximal to the 5′ UTR, like the PTE of SCV (5), reporter constructs were generated containing PEMV 5′ sequence (0 to 89 nt) upstream of the firefly luciferase ORF (F-Luc), followed by the presence or absence of the PEMV 3′ UTR (Fig. 1B). A construct identical to one used in a previous report (49) (i.e., containing the precise PEMV 5′ UTR and 3′ UTR) produced luciferase activity in *Arabidopsis thaliana* protoplasts that was 2.3-fold higher than that found for a construct missing the 3′ UTR (Fig. 1B). Translation was not further enhanced when the 5′ sequence was extended into the p33 ORF to position 38 (5′38+3U). However, extension to position 89 resulted in a nearly 14-fold enhancement in translation over that for constructs containing precise 5′ and 3′ UTRs, and this enhancement required the presence of the 3′ UTR (compare 5′89+0 with 5′89+3U). The different levels of translation were unrelated to the stability of the transcripts (Fig. 1C), and thus reflected differences due to *cis* translation elements.

To determine if enhanced translation was due to a long-distance RNA-RNA interaction linking 5′ and 3′ sequences, electrophoretic mobility shift assays (EMSAs) were performed using the labeled 5′ 89-nt fragment (5′89) and full-length or truncated fragments derived from the PEMV 3′ UTR (Fig. 2A). Full-length 3′ UTR fragment F1 retarded the mobility of 5′89, suggesting that at least one long-distance RNA-RNA interaction occurs *in vitro* (Fig. 2B). Fragment F7, containing only the PTE, did not retard the

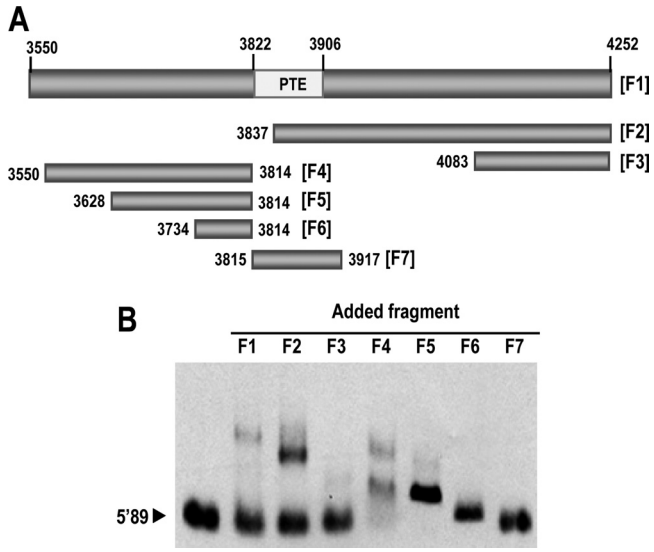

FIG 2 Detection of RNA-RNA interactions by EMSA. (A) Fragments derived from the 3′ UTR that were used for the EMSA analysis. Fragment names are in brackets. (B) The labeled fragment 5′89 was combined with a 10-fold excess of unlabeled 3′ UTR fragments. The position of 5′89 is indicated.

mobility of the 5′89 fragment, supporting the previous report (49) that this element does not appear to engage in any long-distance interaction with 5′-proximal sequences. In contrast, all fragments upstream of the PTE, including the adjacent 80-nt fragment F6, retarded the migration of 5′89. The largest of the upstream fragments, F4, produced a supershift, suggesting that several sequences within this fragment are engaging in RNA-RNA interactions, either with the 5′ fragment or internally. In addition, fragment F2, located mainly downstream of the PTE, contains a sequence that is also capable of interacting with 5′89. These results indicate that multiple RNA-RNA interactions occur *in vitro* between sequences in the 3′ UTR of PEMV and a sequence(s) within the 5′ 89-nt fragment of PEMV.

Mfold (56) and in-line structure probing (40) were used to predict the secondary structure of 5′89 and F6, the shortest fragment that produced a mobility shift. In-line probing reports on self-cleavage of the RNA backbone, which occurs only when the 2′ hydroxyl, backbone phosphate, and oxyanion-leaving group adopt an in-line configuration. This topology exists only if the phosphate-sugar backbone can rotate about the C3′-O3′ and O3′P bonds, which occurs if the base is not constricted by canonical/noncanonical hydrogen bonding. Thus, the amount of backbone cleavage at a specific phosphodiester bond correlates with the flexibility of the nucleotide.

The positions of cleavages in 5′89 (Fig. 3A) are most consistent with the presence of two hairpins (Fig. 3B). The 5′-proximal hairpin, 5H1, contains flexible residues in most of the loop regions, but many stem residues were also susceptible to low to moderate cleavage. To determine if the initiation codon is correctly placed at the base of the 5H1 stem, in-line cleavage of 5′89 was repeated with a fragment containing AU-to-UA transversions in the initiation codon (5′89-mAUG). Of the three residues whose cleavage intensity was altered from that of wt 5′89, one was the altered adenylate and two were located on the opposing side of the stem, consistent with the designated positioning of the initiation codon. The second hairpin, 5H2, contained three flexible residues by in-line probing (74CG and 80C), and all were present in predicted loop regions (Fig. 3B). The terminal loop and closing paired bases of 5H2 contain the sequence UGGC, a motif conserved in known or predicted 5′-proximal hairpin loops that participate in several carmovirus PTE kissing-loop interactions (5).

Mfold suggested that fragment F6 adopts a branched two-hairpin structure with a three-way junction (Fig. 3D) that was also present when the full-length gRNA was folded (data not shown). In-line probing of F6 (Fig. 3C) revealed that most flexible residues are in predicted single-stranded regions, with the exception of residues on both sides of the lower stem of the 3′ side hairpin (3H2) (Fig. 3D). The 5′ side hairpin (3H1) contains an 8-nt apical loop with the conserved carmovirus PTE kissing-loop motif GCCA.

To assay for the functional relevance of the predicted F6 structure, single and compensatory mutations were generated in the luciferase translation reporter construct containing the PEMV 5′89-nt fragment and the 3′ UTR (5′89+3U). As shown in Fig. 3E, a 3-nt alteration that disrupts the bottom stem of the F6 element (BSML) reduced translation of the reporter construct to 25% of the wt level, whereas the inclusion of mutations on the opposite side of this stem, which would reform the stem if the structure is correct (BSMcom), enhanced translation to nearly 75% of the wt level. Similarly, a 2-nt alteration in the upper stem of 3H2 (USML) decreased translation to 12% of the wt level, whereas alteration of residues on the opposing side of the stem, designed to be compensatory if the hairpin is present (USMcom), enhanced translation to 80% of the wt level. These results support the branched, two-hairpin secondary structure shown in Fig. 3D.

Additional mutations were also generated to examine the importance of hairpin 3H2 for the translation of the luciferase construct. ENH5, which increased the size of the terminal loop, reduced translation to 21% of the wt level, and ΔTop, which truncated 3H2 by removing the upper portion of the hairpin, also negatively impacted translation, with levels reduced to 13% of wt levels. These results suggest that 3H2 is important for the translational activity of the F6 element.

To determine if the predicted structure of the F6 element is also functionally relevant within the full-length PEMV gRNA, the BSML, BSMcom, USML, and USMcom mutations were incorporated into constructs containing cDNA corresponding to full-length PEMV, and T7 RNA polymerase-synthesized transcripts were inoculated into *Arabidopsis thaliana* protoplasts. The amount of viral genomic RNA (gRNA) accumulating at 24 hpi was measured by quantitative PCR (qPCR) and was compared with the number of control transcripts containing PEMV gRNA with an alteration converting the GDD RdRp active-site motif to GAA. Accumulation of virus containing BSML and USML was reduced to background (GDD) levels, whereas virus containing compensatory mutations accumulated to 60 to 65% of wt levels. These results, similar to those of the luciferase construct, indicate that the Mfold-predicted branched structure is likely found in both the luciferase reporter RNA transcripts and the wt PEMV gRNA and that this structure functions as a translational enhancer.

The RNA-RNA interaction between 5′89 and fragment F6 results from a kissing-loop interaction between apical hairpin loops. Sequences within 5′89 and the F6 element were analyzed for complementarity that would account for the retarded migration of the two fragments by EMSA. Six nucleotides in the 3H1

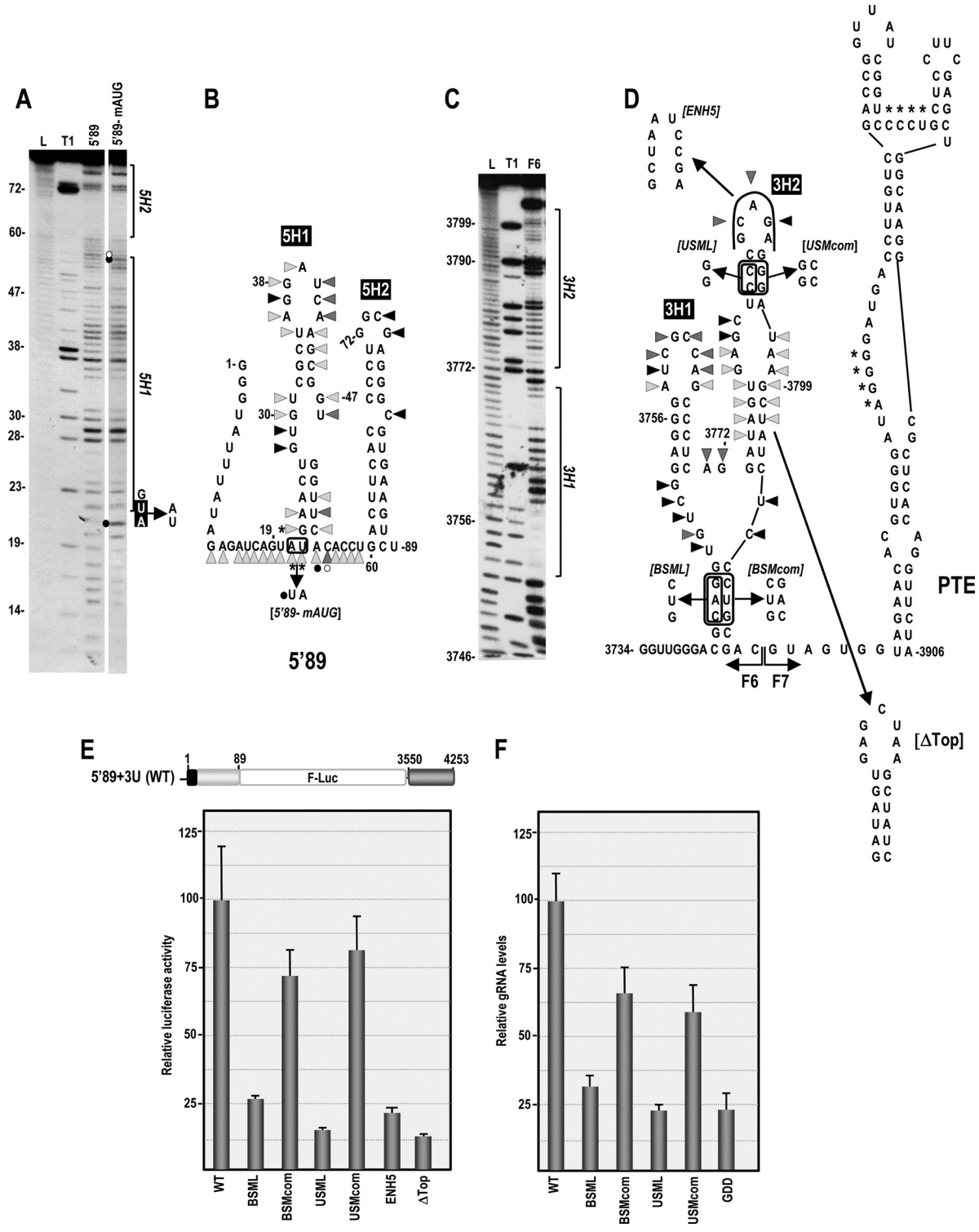

FIG 3 Putative structures of fragments 5′89 and F6. (A) In-line probing of 5′89 and 5′89mAUG, containing a two-residue transversion in the initiation codon. Transcripts were 5′ end labeled and were allowed to self-digest for 14 h at 25°C. The intensities of bands in the in-line cleavage lanes are proportional to the flexibility of the individual residues. Open and filled circles represent residues with reduced or enhanced flexibility, respectively, in 5′89mAUG relative to wt 5′89. L, alkaline-generated ladder; T1, RNase T1 digest of partially denatured fragment 5′89. Numbering at the left is from the 5′ end. The locations of the two likely hairpins are indicated to the right. The locations of the AUG initiation codon and the 2-nt mutation in 5′89mAUG are shown. (B) Putative structure of fragment 5′89. Triangle shading is proportional to the degree of cleavage. Hairpins 5H1 and 5H2 are indicated. Asterisks denote the initiation codon. Open and filled circles denote residues with reduced or enhanced flexibility, respectively, in 5′89mAUG relative to wt 5′89. (C) In-line probing of fragment F6. (D) Putative structure of fragment F6 and fragment F7 containing the adjacent PTE (49). The boundary between fragments F6 and F7 is indicated. The locations of mutations used to support the structure are shown. The names of the mutations are italicized and bracketed. (E) Relative translation of luciferase reporter transcripts containing the mutations shown in panel D. The reporter construct used is diagramed on top. The standard deviation for three replicate experiments is shown. (F) Relative accumulation of wt and mutant full-length PEMV gRNA. Mutations were generated in full-length PEMV RNA-2, and transcripts were inoculated onto protoplasts. Viral levels were determined at 20 hpi by qPCR. GDD, mutant PEMV with GAA replacing the polymerase active-site GDD motif, used as a control. The standard deviation for three replicate experiments is shown.

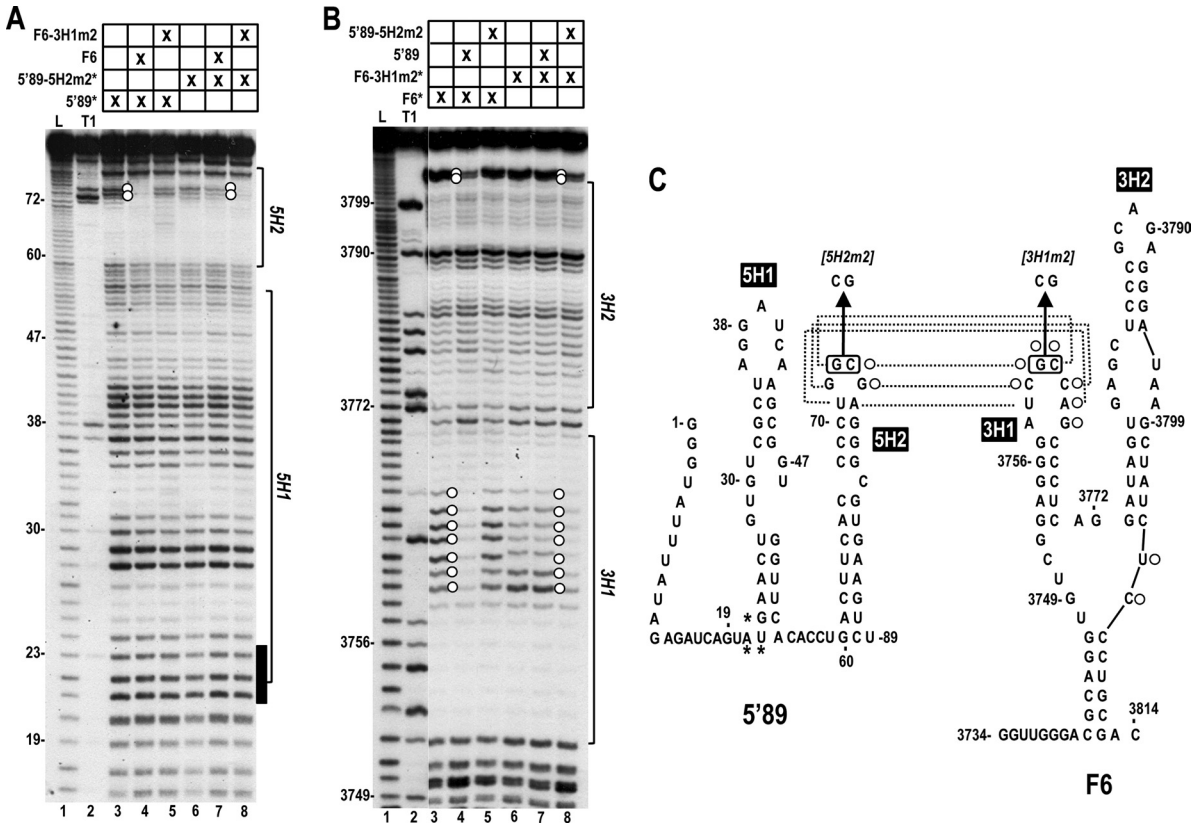

FIG 4 Hairpin 3H1 in fragment F6 engages in a kissing-loop RNA-RNA interaction with 5′89 hairpin 5H2 *in vitro*. (A) In-line probing of labeled wt 5′89 (5′89*) or 5′89 with a two-base alteration in the terminal loop of hairpin 5H2 (5′89–5H2m2*) in the absence or presence of unlabeled fragment F6, or F6 containing a two-base alteration in the terminal loop of hairpin 3H1 (F6–3H1m2). The intensities of the bands in lanes 3 to 8 are proportional to the flexibility of the residues. An asterisk indicates the radioactive fragment. L, alkaline-generated ladder; T1, RNase T1 digest of partially denatured RNA. Open circles denote residues with consistently reduced flexibility when fragments were combined. Filled box to the right denotes the p33 initiation codon. (B) In-line probing of labeled wt F6 (F6*) or F6–3H1m2* in the absence or presence of unlabeled fragment 5′89 or 5′89–5H2m2. (C) Location of residues with reduced flexibility when wt fragments or both mutant fragments were combined. Dotted lines indicate the kissing-loop interaction. The locations of the mutations are indicated. Open circles denote residues whose flexibility is reduced in the presence of the unlabeled fragment.

terminal loop of the F6 element (UCGCCA), including the GCCA motif that is conserved in most PTEs (see Fig. 10), were complementary to sequence in, or adjacent to, the apical loop of 5′89 5H2 (71UGGCGA) (Fig. 4C). To provide support for this putative 5H2–3H1 long-distance interaction, in-line probing was conducted in the presence of both the 5′89 and F6 fragments. Any interfragment RNA-RNA interaction should be discernible by decreased residue flexibility caused by newly constrained paired bases. Addition of unlabeled F6 to labeled 5′89 followed by in-line probing reduced the flexibility of residues 74CG in the 5H2 apical loop (Fig. 4A, lane 4, two adjacent open circles). Addition of F6 containing a 2-nt alteration in the putative interacting sequence in the loop of 3H1 (3761GC to CG; 3H1m2) restored the flexibility of 74CG (Fig. 4A, lane 5). Likewise, addition of wt F6 to labeled 5′89 with a 2-nt mutation in the apical loop of 5H2 that should disrupt the kissing-loop interaction (74CG to GC; 5H2m2) maintained the flexibility of 74GC. When the two mutant fragments were combined, the mutations, designed to be compensatory, reduced the flexibility of 74GC in 5′89.

A similar combination of mutant and wt fragments was used to examine the structure of the F6 element when engaged in the RNA-RNA interaction. When labeled F6 was combined with 5′89, seven of eight residues in the F6 3H1 terminal loop were less flexible (Fig. 4B, lane 4, seven open circles; Fig. 4C, right), as were two residues linking 3H2 with the lower F6 element stem (3803UC). All residues regained their flexibility when either F6 or 5′89 contained mutations in the putative interacting sequences (Fig. 4B, lanes 5 and 7). When mutant F6 and 5′89 were combined, the flexibility of the 3H1 apical loop and 3803UC was again reduced (Fig. 4B, lane 8). These experiments indicate that the RNA-RNA interaction between the fragments *in vitro* involves the apical loops of 5H2 and 3H1.

The RNA-RNA interaction is important for the translation of the reporter construct and the accumulation of the full-length viral genome *in vivo*. To determine if the 5H2–3H1 interaction is important for translation, compensatory mutations 5H2m2 and 3H1m2 were introduced individually or together into the luciferase reporter construct. Transcripts containing the individual mutations reduced translation to less than 14% of wt levels, whereas combining the two mutations restored translation to greater-than-wt levels (Fig. 5B). Since the 5′89 alterations would affect p33 and the p33 portion of the RdRp if incorporated into the full-length virus, the experiment was repeated with single-nucleotide mutations in 5′89 and the F6 element (5H2m1 and 3H1m1, respectively) that were designed not to disrupt the primary sequence of p33. Both single mutations reduced the translation of

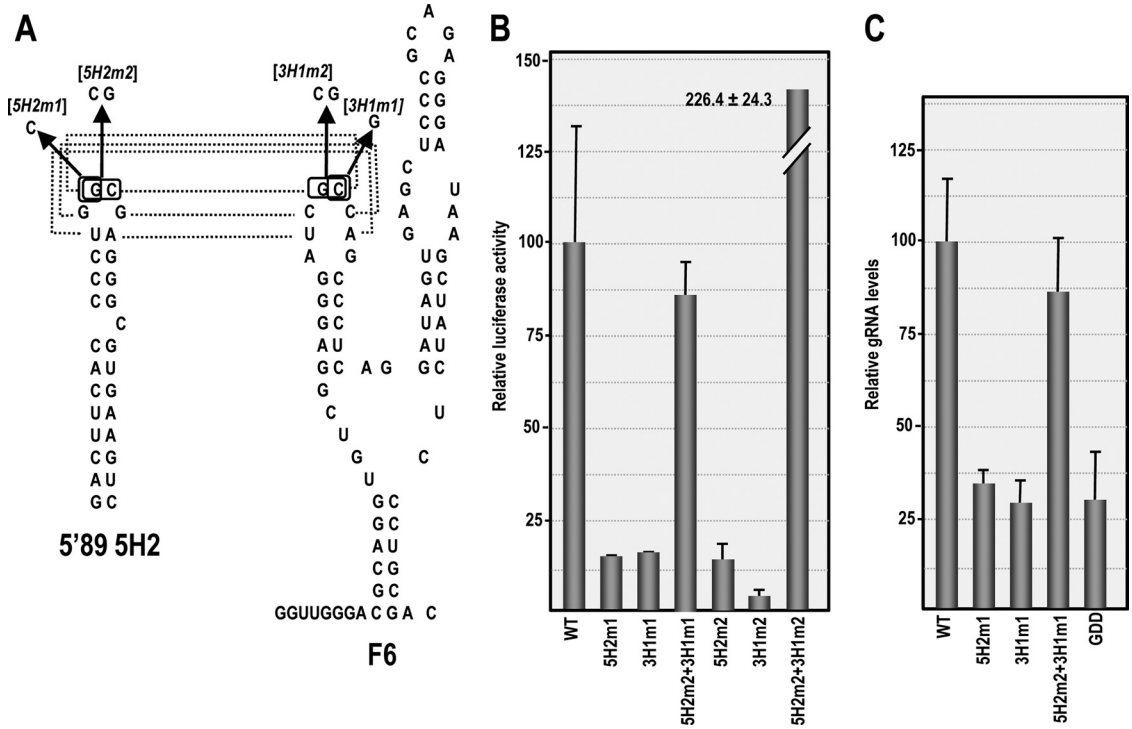

FIG 5 The kissing-loop interaction enhances translation and viral RNA accumulation *in vivo*. (A) Locations of mutations used to test the kissing-loop interaction. The names of the mutations are italicized and bracketed. (B) Relative translation of the luciferase reporter transcripts containing the mutations shown in panel A. The standard deviation for three replicate experiments is shown. The reporter construct used is diagramed in Fig. 3E. (C) Relative accumulation of wt and mutant full-length PEMV. Mutations were generated in full-length PEMV RNA-2, and transcripts were inoculated onto protoplasts. Viral levels were determined 20 hpi by qPCR. GDD, mutant PEMV with GAA replacing the polymerase active-site GDD motif, used as a control. The standard deviation for three replicate experiments is shown.

the reporter construct by 88%, whereas combining the mutations was compensatory, restoring translation to near-wt levels (Fig. 5B). When these single mutations were individually incorporated into the full-length PEMV cDNA, PEMV levels were reduced to background (GDD mutant) levels (Fig. 5C). PEMV accumulation was restored to near-wt levels when both mutations were present in the same transcripts. Altogether, these results support a long-distance RNA-RNA interaction between apical loops of 5H2 and 3H1 that is critical for efficient translation of the reporter construct and accumulation of the viral genome.

The RNA-RNA interaction is multifunctional for translation of the reporter construct. Most 3′ CITEs that bind to translation factors are capable of engaging in a long-distance RNA-RNA interaction (13, 28–31) that would relocate bound elements to the 5′ end. The presence of the F6 element adjacent to the PTE suggested that the RNA-RNA interaction provided by the F6 element might also function to relocate the PTE and bound eIF4E to the 5′ end. If this activity comprises the only function for the F6 element in translation, then eliminating the PTE and disrupting the F6 element's RNA-RNA interaction should lead to similar reductions in translation levels. To investigate this possibility and also explore if any additional 3′ UTR elements are important for translation, we assayed for the effects of deleting regions upstream and downstream of the F6 element on translation of the reporter construct (Fig. 6A). As shown in Fig. 6B, deleting all sequences downstream of the PTE reduced translation by 37%, indicating that either an additional downstream element exists or sequences 3′ of the PTE are necessary for the full function of upstream translational enhancers. Deletion of sequences 5′ of the F6 element had no discernible effect in the absence of the downstream region (compare constructs B, C, and D). Surprisingly, constructs with no sequences downstream of the F6 element (i.e., the PTE was absent) had a level of translational enhancement 2- to 7.5-fold higher than that determined for full-length constructs that were incapable of forming the 3H1–5H2 interaction (Fig. 5B). Inclusion of 237 random bases downstream of the minimal F6 element (construct H) improved translation by 20%, suggesting that either the function(s) of the F6 element is slightly improved or the transcript is more stable when the F6 element is distal to the RNA's 3′ terminus. These results suggest that the long-distance RNA-RNA interaction mediated by the F6 element has an additional role in translation that is independent of assisting in the relocalization of the eIF4E-bound PTE.

The F6 element is predicted to form a 3-D flexible T-shaped structure. To gain information about a possible secondary activity for the F6 element, the element was modeled with two 3-D structure prediction programs. Given the secondary structure of the F6 element shown in Fig. 3D, a preliminary 3-D model was generated with RNA2D3D (24), the program previously used to predict the 3-D structure of the TCV TSS (26). The multibranch loop at the center of the F6 element (M-loop) (Fig. 7A), consisting of the three-way junction with single strands of 5 nt, 2 nt, and 2 nt in the 5′-to-3′ order, was left open, i.e., without the potential interaction at G3772-U3805 bp. The 4-by-3 internal loop (I-loop) in 3H2 was "compactified," extending the upper helix in hairpin 3H2 to include three noncanonical interactions and the 5′ side bulge

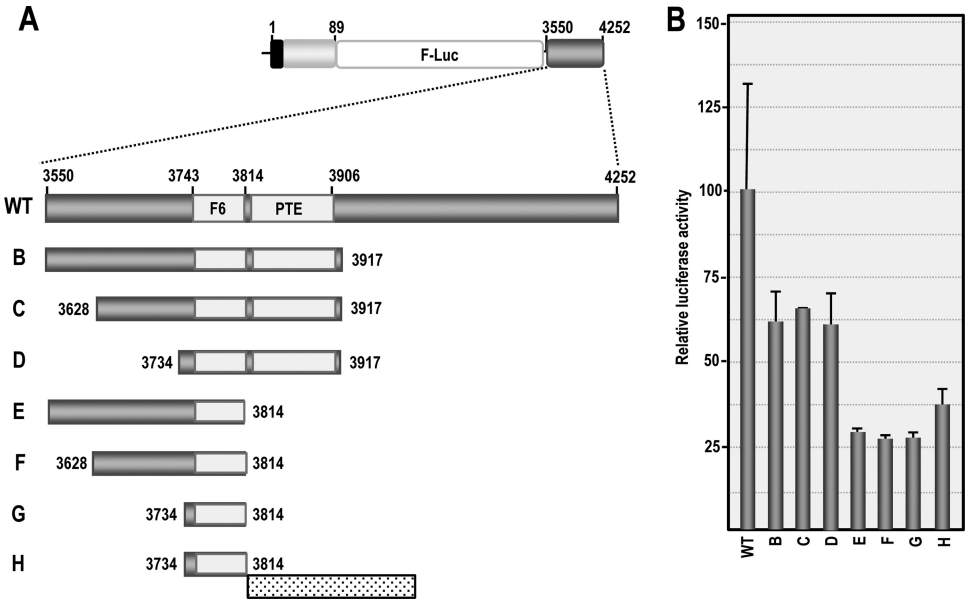

FIG 6 The F6 element enhances translation in the presence and absence of the PTE. (A) Luciferase reporter constructs containing the 5′ 89-nt fragment and various amounts of 3′ UTR sequence were generated. Construct H contains a minimal F6 fragment upstream of a random sequence of 273 nt (dotted box). (B) Relative luciferase activities of the constructs diagramed in panel A. The standard deviation for three replicate experiments is shown.

G3779. The hairpin loops in the arms of 3H1 and 3H2 were also shaped as extensions of the 3′ side of the closing/following helices, which is an option in RNA2D3D. Modeling of the asymmetric M-loop was guided by the supposition that the single strands should follow the flanking helices' geometry as far as possible into the loop. The application of these RNA2D3D functions resulted in a compact T-shaped structure, in which the F6 element's "trunk" (5′-3′) helix and the lower 3H2 arm's helix orient coaxially, as if stacked, with a 2-nt single strand following the helicity of the backbone between them (Fig. 7B, structure A). This structure generally conforms to the "Family A" topology of three-way junctions as presented by Lescoute and Westhof (21). The 3H1 helix is perpendicular to the stacked helix, with the 5-nt single strand between the "trunk" and the 3H1 helices extending the helicity of 3H1.

The T-shaped structure A was also compatible with a transition to a Y-shaped structure, in which the hairpin loop of 3H1 would be in the proximity of the I-loop of 3H2. To narrow down the possibilities for orientation of the two hairpins, this arrangement was explored using the modeling program MCSym (http://www.major.iric.ca/MC-Pipeline/), which builds 3-D models from a database of small structural motifs that are used as building blocks (32). Given the same F6 element secondary-structure descriptor, MCSym produced three major variants, the best of which (by Amber 99 energy, quality scoring available in MCSym, and entropy) (32, 47) was a T-shaped structure (Fig. 7D, structure B) with a general topology identical to that of structure A and within a 7.2 Å root mean square deviation (RMSD) of it, measured with respect to the sugar/backbone C4′ atoms (20, 47).

To explore the stability of structures A and B, both were subjected to at least 50 ns of molecular dynamic (MD) simulation (Fig. 7F and G). The T-shaped structures displayed substantial flexibility within the 3H2 arm due to lower stability of the noncanonical base pairs in the 3H2 internal loop (more pronounced in structure B), which may account for the low-level cleavages within this arm as assayed by in-line probing (Fig. 3B). Arms 3H1 and 3H2 of structure A were moving apart in MD, reaching a near-coaxial orientation, but not stacked, at the simulation points corresponding to the maximum RMSD point or a point near it (Fig. 7F). In structure B, arms 3H1 and 3H2 came close to each other in MD, but not to the point of establishing a stable Y shape or tertiary interaction between the two arms (Fig. 7G). Overall, these MD trajectories indicate that the T-shaped structure is a common prediction and is either the preferred state or an intermediate state.

PEMV structure A was aligned with a phenylalanine tRNA (Protein Data Bank [PDB] code 1EHZ) by overlapping the tRNA acceptor stem backbone and the F6 3H1 hairpin (Fig. 7H). P atoms of the backbones were RMSD-fit for the 71-nt F6 residues 12 to 16 and 24 to 28 and the corresponding 76-nt tRNA residues 66 to 70 and 2 to 6. The RMSD for these 10 pairs of phosphorus atoms was 0.92 Å, denoting a close alignment for these atoms. Although the junction between the 3H1 and 3H2 arms of the F6 element showed considerable flexibility in MD simulations, the overall shape and size of the F6 element and the tRNA were comparable, with substantial overlap found at multiple MD trajectory points. Note that the tRNA's anticodon stem-loop (AC) and the F6 element's 3H2 stem-loop are axially misaligned by almost 180°, reversing the 5′-3′ orientation of the backbone. In addition, the junction between 3H1 and 3H2 in the F6 element is structurally much simpler than the tRNA junction, in which the anticodon stem-loop's axial orientation is "reversed" via the variable size loop and is maintained by tertiary interactions.

The F6 element binds to ribosomes and ribosomal subunits. Since the most stable structure predicted for the F6 element is similar in shape and size to a canonical tRNA as well as resembling the ribosome-binding TCV TSS (26, 41, 57), filter-binding assays were conducted to determine if the F6 element is likewise capable of binding to 80S ribosomes and ribosomal subunits. Whereas yeast ribosomes and ribosomal subunits were previously used to

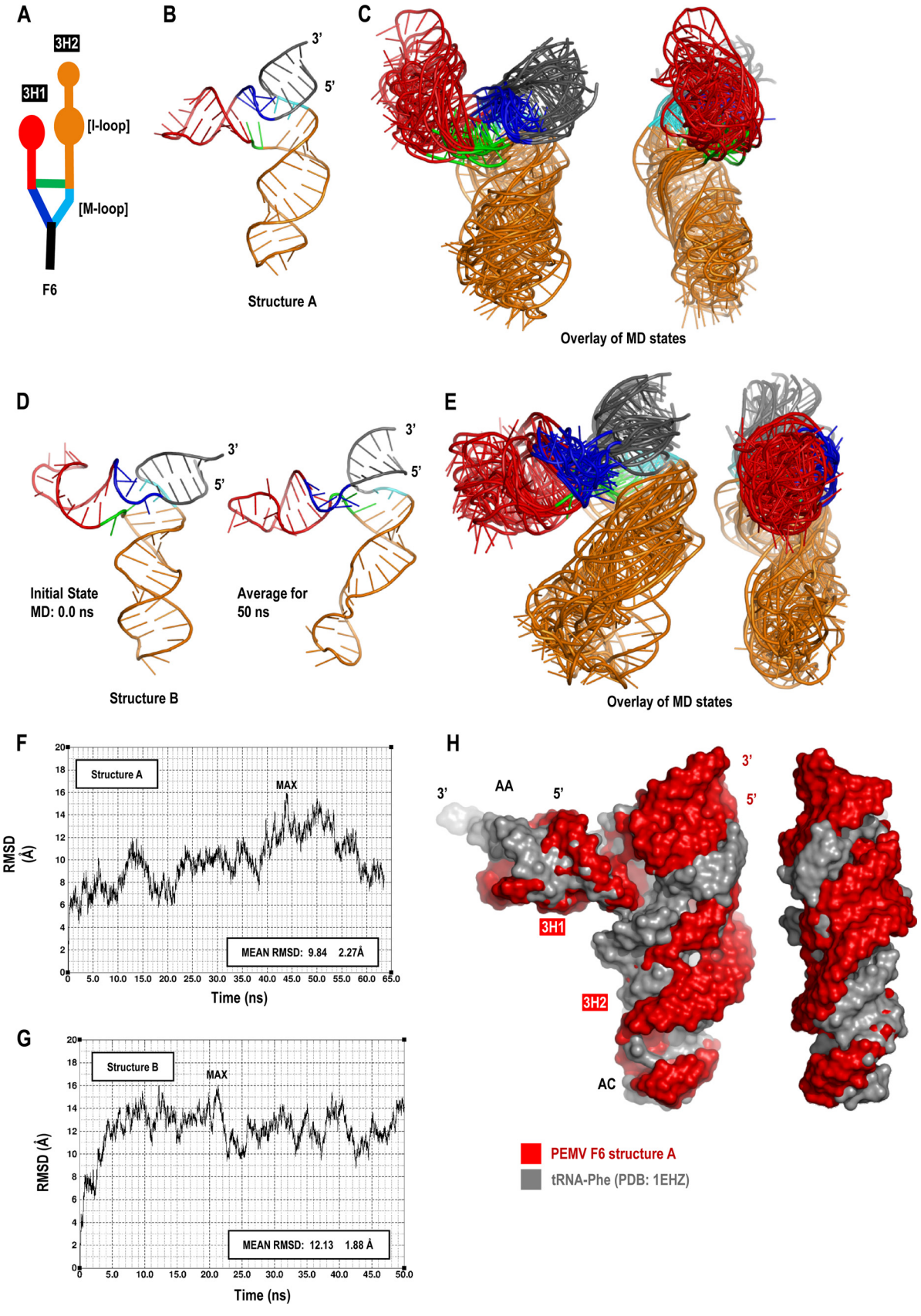

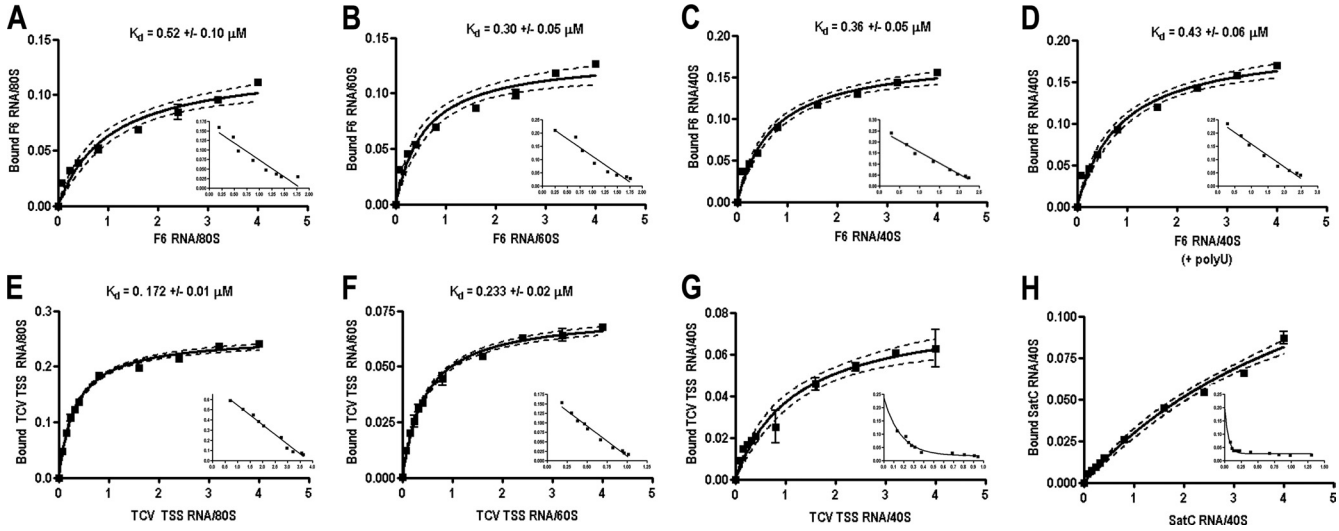

FIG 8 Ribosomes and ribosomal subunits bind to the F6 element and TCV TSS. Two to 60 pmol of labeled F6 was combined with 15 pmol of salt-washed *A. thaliana* 80S ribosomes (A), 60S subunits (B), or 40S ribosomal subunits (C and D), and bound RNA was detected following filtration. Binding of the 40S subunit was conducted in the presence (D) and absence (C) of poly(U). TCV TSS served as a positive control for binding to 80S ribosomes (E) and 60S (F) and 40S (G) subunits. (H) SatC served as a negative control for 40S subunit binding. The saturation binding curves are shown together with Scatchard plots (insets). The similarity in nonlinear Scatchard plots between *satC*/40S subunits and TCV/40S subunits (F) is interpreted as nonspecific ribosome binding for the TCV TSS. For all assays, K_ds were calculated from three independent experiments. Error bars represent standard errors.

assess TCV TSS binding (41), a new protocol was developed for the isolation of *Arabidopsis* ribosomes from protoplasts derived from callus tissue (see Materials and Methods) (V. A. Stupina and A. E. Simon, unpublished data). The TCV TSS bound to *Arabidopsis* 80S ribosomes with a K_d (dissociation constant) of 1.72 μM, which is 2.6-fold better than the level achieved with yeast ribosomes (Fig. 8E). TCV TSS binding to *Arabidopsis* 60S subunits was also greater than that with yeast 60S subunits (K_ds, 0.233 μM and 0.34 μM, respectively), while binding to the 40S subunit remained nonspecific (Fig. 8F and G). A satellite RNA of TCV, *satC*, which is not predicted to form a TSS structure and binds nonspecifically to yeast ribosomes (41), was also not specifically bound by *Arabidopsis* 40S subunits (Fig. 8H).

As with the TCV TSS, PEMV F6 transcripts bound specifically to *Arabidopsis* 80S ribosomes and 60S ribosomal subunits but with reduced efficiency (K_ds, 0.52 μM for 80S ribosomes and 0.30 μM for 60S subunits) (Fig. 8A and B). Unexpectedly, the F6 element also bound specifically to 40S subunits (K_d, 0.36 μM) (Fig. 8C). Binding of the PEMV element to 40S subunits was not significantly affected by the addition of poly(U) (K_d, 0.43 μM), in contrast to the TCV TSS (41), suggesting that the F6 element mainly binds to 40S subunits at a location other than the nonspecific mRNA tunnel (Fig. 8D).

Reduced affinity for ribosomes correlates with reduced translational efficiency. To begin to determine whether ribosome binding is important for efficient translation, transcripts containing mutations (shown in Fig. 3) that altered the structure of the F6 element and reduced translation by 4- to 8-fold were assayed for ribosome binding and the ability to engage in the RNA-RNA interaction (Fig. 9). These mutations, repeated for clarity in Fig. 9A, also included the two compensatory alterations that re-form either the lower stem of the F6 element (BSMcom) or the upper stem of hairpin 3H2 (USMcom). Ribosome binding was analyzed by competitive EMSAs using labeled fragment F6 and *Arabidopsis* 80S ribosomes in the presence and absence of increasing levels of unlabeled wt and mutant F6 fragments. As shown in Fig. 9B and summarized in Fig. 9C, disrupting the upper stem of 3H2 (USML) and re-forming the upper stem (USMcom) had no discernible effect on ribosome binding. In contrast, mutations that either disrupted the lower stem of the F6 element (BSML), enlarged the 3H2 terminal loop (ENH5), or truncated 3H2 (ΔTop) reduced ribosome binding by 2.9-, 2.0-, or 3.6-fold, respectively, based on their I_{50} (relative level of competitor needed to reduce ribosome binding to the labeled fragment by 50%). BSMcom, which reformed the lower stem, restored ribosome binding to near-wt levels. SatC, used as a negative control, was noncompetitive, as expected.

To determine if these mutations might exert a negative effect on translation by affecting the critical RNA-RNA interaction,

FIG 7 The F6 element is predicted to assume a T-shaped structure. (A) Colored representation of the F6 element. (B) The 3-D structure (structure A) modeled by RNA2D3D (24). Color coding is in agreement with the scheme shown in panel A. (C) Overlay (minimum RMSD with respect to the initial equilibrated state) of molecular dynamics (MD) states corresponding to the selected peaks and troughs in the RMSD plot for structure A shown in panel F. (D) (Left) Lowest free-energy 3-D structure predicted by MCSym (32) (structure B). (Right) Minimized average structure for the entire 50-ns MD trajectory. (E) Overlay of MD states for structure B. The dynamic behavior of this model brings arms 3H1 and 3H2 in proximity to each other, forming a "Y" shape, but without inducing tertiary interactions between the arms. At the trajectory points corresponding to the prominent troughs in the RMSD plot shown in panel G, such as at the ~42.5-ns point, the overall shape of structure B returns to the "T" topology. (F) RMSD plot for the 64-ns MD trajectory for structure A, in which RMSD values were calculated for all the RNA molecule atoms (solvent and ions excluded) relative to the initial MD state, i.e., RNA molecule coordinates following equilibration in solvent. (G) RMSD plot for the 50-ns MD trajectory for structure B. (H) Alignment of the initial energy-minimized PEMV F6 structure A (red) with a phenylalanine tRNA (PDB code 1EHZ) (gray) based on PEMV 3H1–tRNA acceptor stem (AA) backbone alignment. AC, anticodon stem of the tRNA.

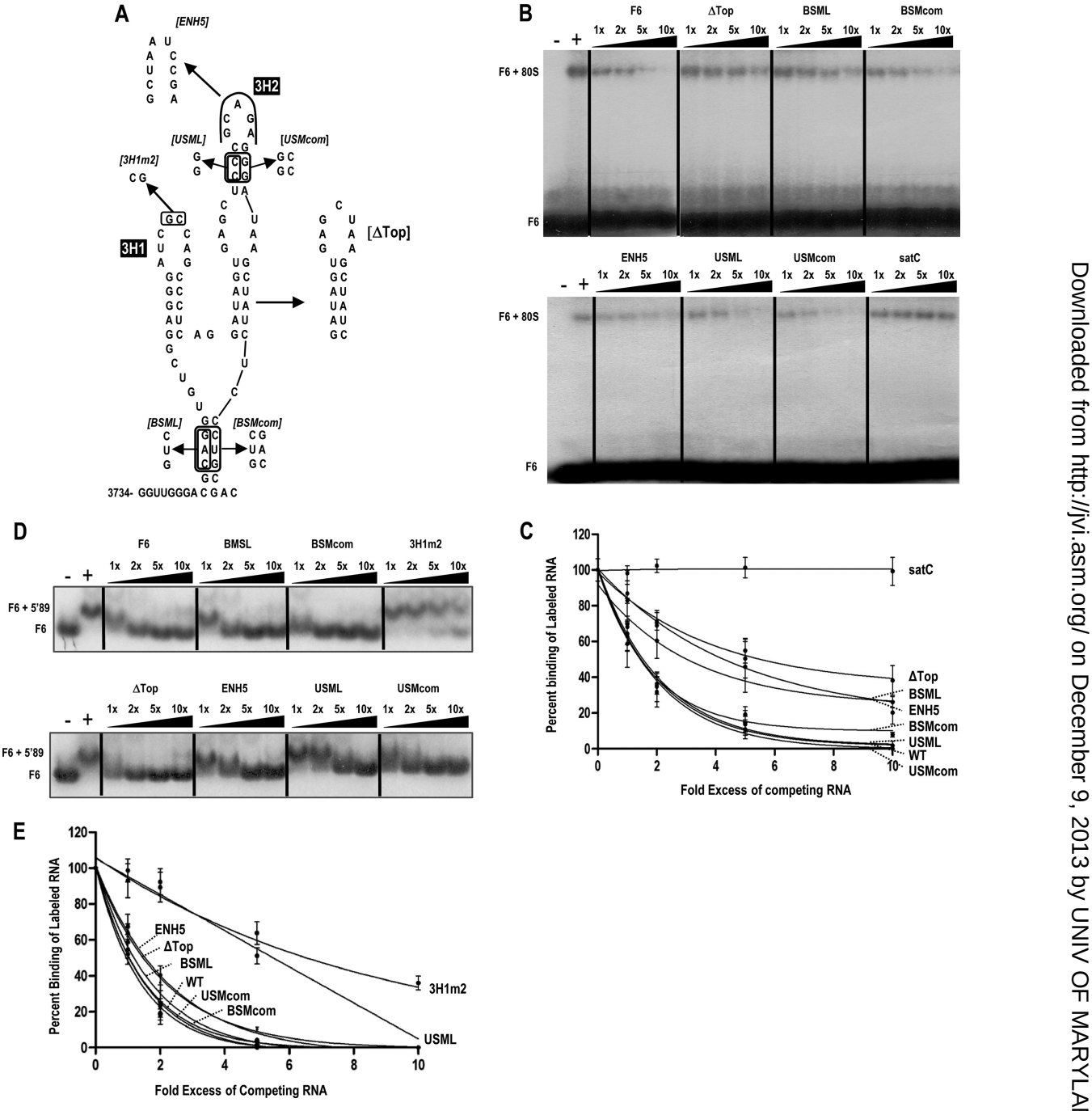

FIG 9 Binding affinities of F6 mutants to 80S ribosomes and 5′89 determined by competitive EMSAs. (A) The F6 mutants shown in Fig. 3D were tested for their abilities to compete for 80S ribosome binding (B) or 5′89 binding (D) in competitive EMSAs using a [γ-32p]ATP-labeled wt F6 fragment and an increasing molar excess of unlabeled competitor RNAs. (C and E) The intensity of the shifted signal was quantified and normalized to that of the shifted signal obtained in the absence of any competitor RNAs. These values were plotted on the *y* axis against the fold excess of unlabeled competitor RNAs. Data were obtained from three independent experiments; error bars represent standard errors. SatC and 3H1m1 served as negative controls for 80S ribosome binding and 5′89 binding, respectively.

competitive EMSAs were performed using labeled fragment F6 and unlabeled fragment 5′89, in the presence and absence of increasing levels of unlabeled wt and mutant F6 fragment (Fig. 9D). F6 containing 3H1m2, which directly inhibits the RNA-RNA interaction by altering the 3H1 loop, was poorly competitive, as expected, with an increase in the I_{50} of 6-fold over that for the wt. USML, the sole mutation that disrupts the structure of the F6 element and reduced translation without affecting ribosome binding, was also poorly competitive, with an I_{50} 5-fold greater than that for the wt (Fig. 9E). All other mutations had no significant effect on the RNA-RNA interaction, as measured by this EMSA. Altogether, these results are consistent with the F6 element

having at least two functions in translation: participating in a long-distance RNA-RNA interaction with 5H2 and also binding to ribosomes and ribosomal subunits.

DISCUSSION

3′ CITEs replace the need for highly structured 5′ IRESs, allowing plant viruses that engage in cap-independent translation to reduce the sizes of their genomes by forgoing mechanisms requiring extensive 5′ UTR sequences to attract ribosomes. 3′ CITEs are currently divided into six major classes based mainly on secondary structure and association with particular translation initiation factors, such as eIF4E, eIF4F, or eIF4G (10, 18, 28, 30, 49). The 3-D structures of 3′ CITEs and how they contribute to attracting ribosomes to the template are subjects of intense speculation centering on their additional participation in long-distance RNA-RNA interactions that relocalize the 3′ CITE and bound factor to the 5′ end, which is thought to facilitate 43S subunit entry and subsequent scanning to the initiation codon (13, 16, 17, 27, 43, 51). Support for this molecular model was recently obtained for the 3′ CITE of the tombusvirus *Maize necrotic streak virus* (31). This I-shaped CITE binds to both eIF4E and eIF4G subunits when associated in the eIF4F complex and simultaneously engages in a long-distance RNA-RNA interaction that leads to 43S subunit entry at the 5′ end. The TCV TSS represents a substantially different class of 3′ CITEs, enhancing translation by using tRNA mimicry to attract ribosomes or ribosomal subunits in the absence of any detectable long-distance RNA-RNA interaction (26, 41, 57). Instead, a ribosome-mediated "bridge" has been suggested to form when a 40S subunit interacting at a polypyrimidine-rich segment in the TCV gRNA 5′ UTR joins with a 60S subunit bound to the TSS (42), relocalizing the 60S subunit to the 5′ end.

In this report, we identify a novel 3′ CITE in PEMV that contains properties associated with different classes of translational enhancers. Like I-shaped, Y-shaped, and BTE-type classes of 3′ CITEs found in some members of the *Tombusviridae* (13, 14, 16, 17, 27, 36, 43, 51), the F6 element engages in a long-distance kissing-loop interaction with a 5′ hairpin (5H2), which is essential for efficient translation and virus accumulation (Fig. 4 and 5). Our original speculation was that the 5H2–3H1 interaction was specifically required to bring the adjacent eIF4E-bound PTE to the 5′ end to assist in the 5′ entry of 43S subunits. This speculation was based on reports that the SCV PTE, but not the PEMV PTE, circularizes the template through an associated RNA-RNA interaction (5, 49) and that this long-distance interaction appears to be conserved for other PTEs. The absence of a similar interaction for the PEMV PTE suggested that the F6 element likely functioned by serving as the necessary bridge to relocate the PTE–eIF4E complex to the 5′ end. Unexpectedly, however, elimination of the long-distance RNA-RNA interaction was more detrimental to translation than deletion of the PTE (Fig. 5 and 6), suggesting that the kissing-loop interaction is required for an activity in addition to a strictly PTE relocalization function.

Our finding that the F6 element binds to 80S ribosomes and 40S and 60S ribosomal subunits (Fig. 8), suggested that this second function is associated with its ribosome binding activity. Evidence for a contribution of ribosome binding to translation was provided by analysis of mutations designed to disrupt the structure of the F6 element without disrupting the portion of the structure (3H1) engaged in the RNA-RNA interaction. With one exception, mutations disrupting hairpin 3H2 or the lower stem of the F6 element reduced both ribosome binding and the translation of the luciferase reporter construct (Fig. 3 and 9), while having little or no effect on the RNA-RNA interaction. The one exception (USLM), which disrupted the stem of 3H2, had no discernible effect on ribosome binding but did affect the RNA-RNA interaction by an unknown mechanism. Thus, all F6 mutations that substantially reduced translation reduced either ribosome binding or the RNA-RNA interaction, strongly suggesting that both functions are important for translational enhancement. However, we cannot rule out the possibility that an additional F6-associated activity was responsible for the reduced translation of the F6 mutants or that the *in vitro* EMSA for the RNA-RNA interaction was more permissive than the interaction within the gRNA *in vivo*. Nevertheless, the likely importance of both functions suggests the intriguing possibility that the adjacent PTE–eIF4E complex functions in translational enhancement by enhancing ribosome binding to the F6 element, which would be expected to require additional translation factors, such as eIF3 and eIF4G.

While both the F6 element and the TCV TSS represent internal 3′ ribosome-binding elements, they differ in many noteworthy aspects, including the exclusive ability of the F6 element to (i) bind 40S subunits and (ii) engage in the RNA-RNA interaction. In addition, the positioning of the TCV TSS near the 3′ terminus allows it to partake in the conformational shift that restricts translation when sufficient RdRp is synthesized (53). It is currently unknown whether the F6 element is similarly connected with shifting between these two incompatible activities. Ribosome binding by the F6 element and TSS differs from the well-characterized ribosome-binding elements involved in translational reinitiation of influenza B virus segment 7 RNA and expression of *Caliciviridae* protein VP2 (23, 34). In the latter examples, 40S subunits are attracted to an RNA motif just upstream of the first ORF stop site through possible RNA base-pairing interactions with helix 26 of 18S rRNA, assisted by eIF3. This mechanism is suggested to keep 40S subunits tethered to the bicistronic RNA to allow for reinitiation on the downstream ORF (34). In contrast, ribosome binding to the PEMV and TCV 3′ UTR elements occurs without a need to translate a downstream ORF and may instead be important for ribosome recycling and reinitiation at the 5′ end of the template by keeping terminating ribosomes and/or dissociated ribosomal subunits from diffusing away from the template.

Molecular modeling of the F6 element using either RNA2D3D or MCSym suggests that the F6 element adopts a stable T-shaped conformation (26, 57) that is similar to the TCV TSS despite differences in secondary structure. In contrast to TCV TSS hairpin H4a, which is engaged in a pseudoknot interaction, the 3-D models of the F6 element and the MD results predict that the loop residues of the similarly positioned 3H1 are mobile and oriented outward from the loop, and thus are free to engage in outside interactions, which likely contributes to their participation in the stable kissing-loop interaction. In addition, the entire 3H1 branch shows substantial mobility in MD simulations of the 3-D models, also potentially aiding in the search for a kissing-loop partner. The 3-D shape similarity between the F6 element and the TCV TSS and the functional similarity in binding to ribosomes suggest that the F6 element is a second TSS-type element. However, to distinguish the PEMV element from the TCV TSS, the F6 element will be designated a kissing-loop or "kl" TSS (kl-TSS).

The branched, two-hairpin secondary structure of the kl-TSS is

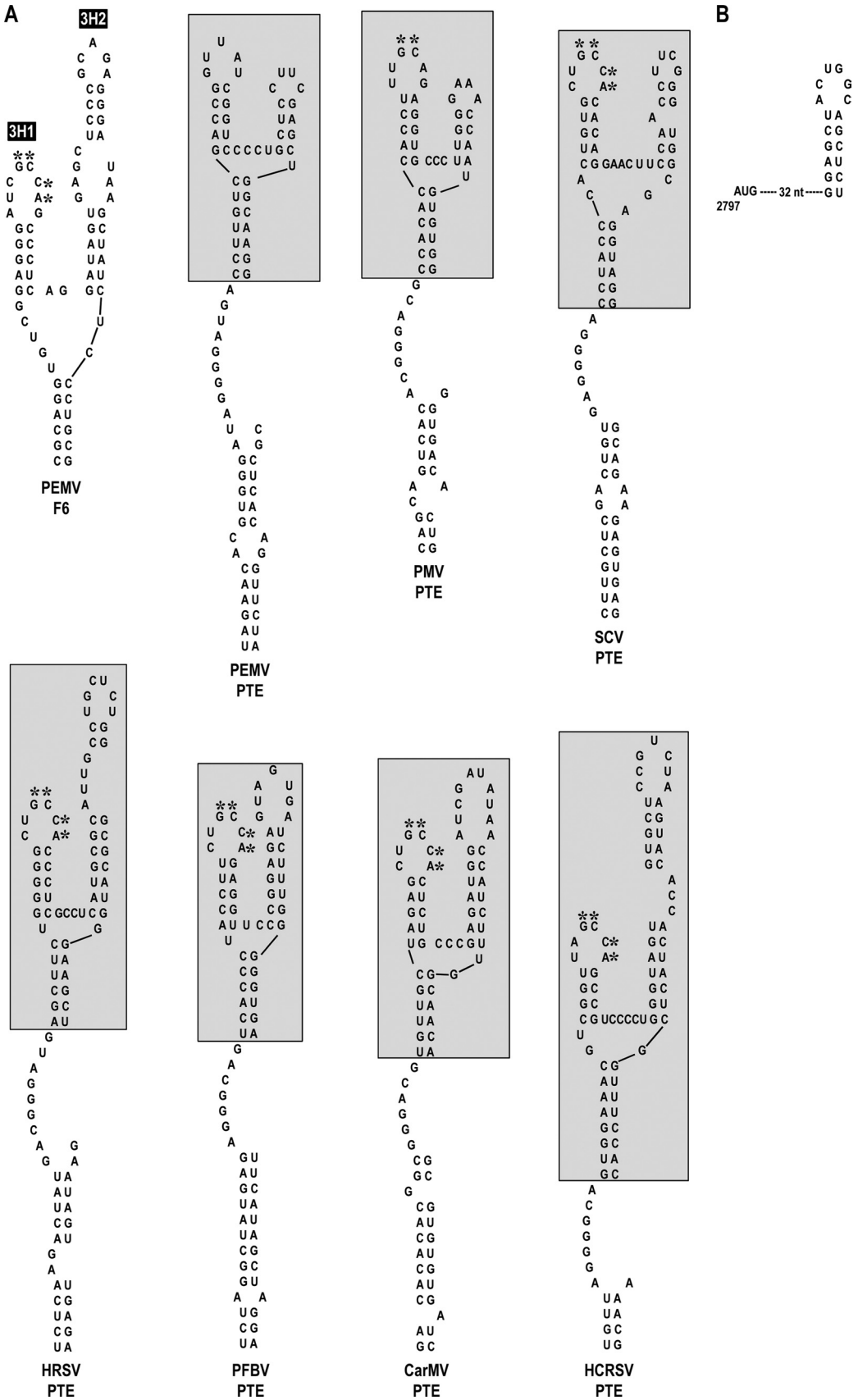

FIG 10 The F6 element resembles the upper portion of a PTE. (A) Six PTE structures are shown for comparison along with the PEMV PTE. The upper portion of the PTE (boxed) contains a similar branched three-way junction. With the exception of the PEMV PTE, the 5′ side hairpins of all PTE are known or predicted to engage in a long-distance RNA-RNA interaction with hairpin terminal loops located either in the 5′ UTR or in nearby coding regions (2, 5, 48). Conserved sequences in the F6 element and the PTE are denoted by asterisks. The PEMV PTE does not contain these conserved sequences. (B) Possible 3H1-interacting sequence in the p26/p27 ORF.

topologically similar to the upper portion of PTEs from three genera of viruses within the *Tombusviridae* (Fig. 10A). The 5′-side hairpins from both the F6 element and 6 of 7 PTEs have 5-bp stems, and all but 1 have apical loops containing the conserved motif GCCA. All PTE 5′-side hairpins (other than that of the PEMV PTE) have been shown to participate, or are capable of participating, in long distance RNA-RNA kissing-loop interactions with apical loops of hairpins located either at the 5′ terminus of the gRNA or near the 5′ end of the 5′-proximal ORF, as well as with hairpins within the 5′ UTR of their shorter sgRNA (5). For PEMV, a hairpin with an apical loop capable of interacting with 3H1 is also located just within the p26/p27 ORFs (Fig. 10B). The lower stem of the F6 element and the equivalent stem of PTE are also similar in length (6 of 7 are 6 bp), while the right-side hairpins (5H2-equivalent) in all PTEs are highly variable in size and sequence. This similarity at the secondary-structure level, combined with similar abilities to engage in long distance RNA-RNA interactions using conserved sequences, suggests that the kl-TSS may have originated as a "truncated" PTE. However, the T-shaped structure predicted for the kl-TSS differs from the recent molecular model of the PEMV PTE, which positioned the 3H1-equivalent stem coaxially stacked onto the lower stem, permitting the formation of a possible pseudoknot that is predicted to dock with eIF4E and that is likely found in other PTEs that are competitive with the PEMV PTE for eIF4E binding (48). Interestingly, we have recently determined that the SCV PTE does not compete with the kl-TSS for 80S ribosome binding (F. Gao and A. E. Simon, unpublished data).

In conclusion, the kl-TSS represents a unique ribosome-binding, 3′ CITE that engages in a long-distance RNA-RNA interaction with the 5′ end. The PEMV PTE, unlike all other PTEs so far identified, does not appear to participate in any long-distance RNA-RNA interaction. Rather, this PTE function has been "transferred" to the upstream, adjacent kl-TSS, which resembles a truncated PTE. The kl-TSS is missing one of the partner sequences necessary to form the PTE pseudoknot, thus allowing it to adopt a tRNA-shaped structure that is capable of binding to ribosomes and ribosomal subunits. This discovery of a second solution to forming an internal tRNA-shaped structure opens up the possibility that TSS-type elements may be found in other viral or mRNA 3′ UTRs that require high-level translation of products.

ACKNOWLEDGMENTS

This work was supported by grants from the U.S. Public Health Service (GM 061515-05A2/G120CD and GM 061515-07S1) and NSF (MCB 1157906) to A.E.S. This publication has been funded in part with federal funds from the Frederick National Laboratory for Cancer Research, National Institutes of Health, under contract HHSN 261200800001E, to W.K. This research was supported in part by the Intramural Research Program of the National Institutes of Health, Frederick National Laboratory for Cancer Research, Center for Cancer Research, to B.A.S.

The content of this publication does not necessarily reflect the views or policies of the Department of Health and Human Services, nor does mention of trade names, commercial products, or organizations imply endorsement by the U.S. Government.

REFERENCES

1. **Baerenfaller K, et al.** 2008. Genome-scale proteomics reveals *Arabidopsis thaliana* gene models and proteome dynamics. Science **320**:938–941.
2. **Batten JS, Desvoyes B, Yamamura Y, Scholthof KBG.** 2006. A translational enhancer element on the 3′-proximal end of the Panicum mosaic virus genome. FEBS Lett. **580**:2591–2597.
3. **Berendsen HJC, Postma JPM, van Gunsteren WF, DiNola A, Haak JR.** 1984. Molecular dynamics with coupling to an external bath. J. Chem. Phys. **81**:3684–3690.
4. **Case DA, et al.** 2008. AMBER 10. University of California, San Francisco.
5. **Chattopadhyay M, Shi K, Yuan X, Simon AE.** 2011. Long-distance kissing loop interactions between a 3′ proximal Y-shaped structure and apical loops of 5′ hairpins enhance translation of Saguaro cactus virus. Virology **417**:113–125.
6. **Demler SA, Rucker DG, de Zoeten GA.** 1993. The chimeric nature of the genome of pea enation mosaic virus: the independent replication of RNA 2. J. Gen. Virol. **74**(Pt 1):1–14.
7. **de Moor CH, Meijer H, Lissenden S.** 2005. Mechanisms of translational control by the 3′ UTR in development and differentiation. Semin. Cell Dev. Biol. **16**:49–58.
8. **Doudna JA, Sarnow P.** 2007. Translation initiation by viral internal ribosome entry sites, p 129–154. *In* Mathews M, Sonenberg N, Hershey JWB (ed), Translational control in biology and medicine. Cold Spring Harbor Laboratory Press, Cold Spring Harbor, NY.
9. **Dreher TW.** 1999. Functions of the 3′-untranslated regions of positive strand RNA viral genomes. Annu. Rev. Phytopathol. **37**:151–174.
10. **Dreher TW, Miller WA.** 2006. Translational control in positive strand RNA plant viruses. Virology **344**:185–197.
11. **Elroy-Stein O, Merrick WC.** 2007. Translation initiation via cellular internal ribosome entry sites. Cold Spring Harbor Monogr. Ser. **48**:155–172.
12. **Essmann U, et al.** 1995. A smooth particle mesh EWALD method. J. Chem. Phys. **103**:8577–8593.
13. **Fabian MR, White KA.** 2006. Analysis of a 3′-translation enhancer in a tombusvirus: a dynamic model for RNA-RNA interactions of mRNA termini. RNA **12**:1304–1314.
14. **Guo L, Allen EM, Miller WA.** 2001. Base-pairing between untranslated regions facilitates translation of uncapped, nonpolyadenylated viral RNA. Mol. Cell **7**:1103–1109.
15. **Jackson RJ, Hellen CU, Pestova TV.** 2010. The mechanism of eukaryotic translation initiation and principles of its regulation. Nat. Rev. Mol. Cell Biol. **11**:113–127.
16. **Karetnikov A, Keranen M, Lehto K.** 2006. Role of the RNA2 3′ nontranslated region of Blackcurrant reversion nepovirus in translational regulation. Virology **354**:178–191.
17. **Karetnikov A, Lehto K.** 2008. Translation mechanisms involving long-distance base pairing interactions between the 5′ and 3′ non-translated regions and internal ribosomal entry are conserved for both genomic RNAs of Blackcurrant reversion nepovirus. Virology **371**:292–308.
18. **Kneller EL, Rakotondrafara AM, Miller WA.** 2006. Cap-independent translation of plant viral RNAs. Virus Res. **119**:63–75.
19. **Kuersten S, Goodwin EB.** 2003. The power of the 3′ UTR: translational control and development. Nat. Rev. Genet. **4**:626–637.
20. **Laederach A, Chan JM, Schwartzman A, Willgohs E, Altman RB.** 2007. Coplanar and coaxial orientations of RNA bases and helices. RNA **13**:643–650.
21. **Lescoute A, Westhof E.** 2006. Topology of three-way junctions in folded RNAs. RNA **12**:83–93.
22. **Liu J.** 2008. Control of protein synthesis and mRNA degradation by microRNAs. Curr. Opin. Cell Biol. **20**:214–221.
23. **Luttermann C, Meyers G.** 2007. A bipartite sequence motif induces translation reinitiation in feline calicivirus RNA. J. Biol. Chem. **282**:7056–7065.
24. **Martinez HM, Maizel JV, Shapiro BA.** 2008. RNA2D3D: a program for generating, viewing, and comparing 3-dimensional models of RNA. J. Biomol. Struct. Dyn. **25**:669–683.
25. **Martinez-Salas E, Pacheco A, Serrano P, Fernandez N.** 2008. New insights into internal ribosome entry site elements relevant for viral gene expression. J. Gen. Virol. **89**:611–626.
26. **McCormack JC, et al.** 2008. Structural domains within the 3′ untranslated region of Turnip crinkle virus. J. Virol. **82**:8706–8720.
27. **Meulewaeter F, et al.** 2004. Conservation of RNA structures enables TNV and BYDV 5′ and 3′ elements to cooperate synergistically in cap-independent translation. Nucleic Acids Res. **32**:1721–1730.
28. **Miller WA, Wang Z, Treder K.** 2007. The amazing diversity of cap-independent translation elements in the 3′-untranslated regions of plant viral RNAs. Biochem. Soc. Trans. **35**:1629–1633.
29. **Miller WA, White KA.** 2006. Long-distance RNA-RNA interactions in plant virus gene expression and replication. Annu. Rev. Phytopathol. **44**:447–467.

30. **Nicholson BL, White KA.** 2011. 3′ cap-independent translation enhancers of positive-strand RNA plant viruses. Curr. Opin. Virol. **1**:373–380.
31. **Nicholson BL, Wu BD, Chevtchenko I, White KA.** 2010. Tombusvirus recruitment of host translational machinery via the 3′ UTR. RNA **16**: 1402–1419.
32. **Parisien M, Major F.** 2008. The MC-Fold and MC-Sym pipeline infers RNA structure from sequence data. Nature **452**:51–55.
33. **Pestova TV, Lorsch JR, Hellen CUT.** 2007. The mechanism of translation initiation in eukaryotes, p 87–128. *In* Mathews MB, Sonenberg N, Hershey JWB (ed), Translational control in biology and medicine. Cold Spring Harbor Laboratory Press, Cold Spring Harbor, NY.
34. **Powell ML.** 2010. Translational termination-reinitiation in RNA viruses. Biochem. Soc. Trans. **38**:1558–1564.
35. **Ryabov EV, Robinson DJ, Taliansky M.** 2001. Umbravirus-encoded proteins both stabilize heterologous viral RNA and mediate its systemic movement in some plant species. Virology **288**:391–400.
36. **Shen RZ, Miller WA.** 2004. The 3′ untranslated region of tobacco necrosis virus RNA contains a barley yellow dwarf virus-like cap-independent translation element. J. Virol. **78**:4655–4664.
37. **Skaf JS, Demler SA, de Zoeten GA.** 1999. Pea enation mosaic virus, p 1191–1196. *In* Webster RG, Granoff A (ed), Encyclopedia of virology. Academic Press, London, United Kingdom.
38. **Sonenberg N.** 2008. eIF4E, the mRNA cap-binding protein: from basic discovery to translational research. Biochem. Cell Biol. **86**:178–183.
39. **Sonenberg N, Hinnebusch AG.** 2009. Regulation of translation initiation in Eukaryotes: mechanisms and biological targets. Cell **136**:731–745.
40. **Soukup GA, Breaker RR.** 1999. Relationship between internucleotide linkage geometry and the stability of RNA. RNA **5**:1308–1325.
41. **Stupina VA, et al.** 2008. The 3′ proximal translational enhancer of Turnip crinkle virus binds to 60S ribosomal subunits. RNA **14**:2379–2393.
42. **Stupina VA, Yuan X, Meskauskas A, Dinman JD, Simon AE.** 2011. Ribosome binding to a 5′ translational enhancer is altered in the presence of the 3′ UTR in cap-independent translation of Turnip crinkle virus. J. Virol. **85**:4638–4653.
43. **Truniger V, Nieto C, Gonzalez-Ibeas D, Aranda M.** 2008. Mechanism of plant eIF4E-mediated resistance against a *Carmovirus* (*Tombusviridae*): cap-independent translation of a viral RNA controlled in *cis* by an (a)virulence determinant. Plant J. **56**:716–727.
44. **Vaughn JN, Ellingson SR, Mignone F, von Arnim A.** 2012. Known and novel post-transcriptional regulatory sequences are conserved across plant families. RNA **18**:368–384.
45. **Vogel C, et al.** 2010. Sequence signatures and mRNA concentration can explain two-thirds of protein abundance variation in a human cell line. Mol. Syst. Biol. **6**:400. doi:10.1038/msb.2010.59.
46. **Vogel C, Marcotte EM.** 2012. Insights into the regulation of protein abundance from proteomic and transcriptomic analyses. Nat. Rev. Genet. **13**:227–232.
47. **Wang J, Cieplak P, Kollman PA.** 2000. How well does a restrained electrostatic potential (RESP) model perform in calculating conformational energies of organic and biological molecules? J. Comput. Chem. **21**:1049–1074.
48. **Wang Z, Parisien M, Scheets K, Miller WA.** 2011. The cap-binding translation initiation factor, elF4E, binds a pseudoknot in a viral cap-independent translation element. Structure **19**:868–880.
49. **Wang ZH, Treder K, Miller WA.** 2009. Structure of a viral cap-independent translation element that functions via high affinity binding to the eIF4E subunit of eIF4F. J. Biol. Chem. **284**:14189–14202.
50. **Wells SE, Hillner PE, Vale RD, Sachs AB.** 1998. Circularization of mRNA by eukaryotic translation initiation factors. Mol. Cell **2**:135–140.
51. **Xu W, White KA.** 2009. RNA-based regulation of transcription and translation of aureusvirus subgenomic mRNA1. J. Virol. **83**:10096–10105.
52. **Yuan X, Shi K, Simon AE.** 2012. A local, interactive network of 3′ RNA elements supports translation and replication of Turnip crinkle virus. J. Virol. **86**:4065–4081.
53. **Yuan XF, Shi KR, Meskauskas A, Simon AE.** 2009. The 3′ end of Turnip crinkle virus contains a highly interactive structure including a translational enhancer that is disrupted by binding to the RNA-dependent RNA polymerase. RNA **15**:1849–1864.
54. **Yuan XF, Shi KR, Young MYL, Simon AE.** 2010. The terminal loop of a 3′ proximal hairpin plays a critical role in replication and the structure of the 3′ region of Turnip crinkle virus. Virology **402**:271–280.
55. **Zhang JC, Zhang GH, Guo R, Shapiro BA, Simon AE.** 2006. A pseudoknot in a preactive form of a viral RNA is part of a structural switch activating minus-strand synthesis. J. Virol. **80**:9181–9191.
56. **Zuker M.** 2003. Mfold web server for nucleic acid folding and hybridization prediction. Nucleic Acids Res. **31**:3406–3415.
57. **Zuo XB, et al.** 2010. Solution structure of the cap-independent translational enhancer and ribosome-binding element in the 3′ UTR of turnip crinkle virus. Proc. Natl. Acad. Sci. U. S. A. **107**:1385–1390.